Multidisciplinary Design Optimization of Reusable Launch Vehicles

A. Cusick* & K. Kontis[†]

School of Engineering, University of Glasgow, Scotland

M. Nikbay[‡]

Faculty of Aeronautics and Astronautics, Istanbul Technical University, Turkey

Reusable launch vehicles have once again become an attractive proposition, due to recent advancements in technology, and the opportunity to massively expand our accessibility to space. This paper discusses the optimization software under ongoing development at the University of Glasgow, that can be applied to such vehicles. Considering the diversity of previous and existing concepts, this work seeks to rapidly produce novel configurations using low-fidelity analysis methods. At present, surface inclination methods for high-speed aerodynamic computation are coupled with a simple six degree-of-freedom finite element beam model. The resulting aerostructural system is then utilized in a population based design optimization framework. Discussions of these methodologies are provided, along with an overall outline of their combination in a typical large design space optimization. Descriptions of the design variables employed are presented, along with an analysis of the methods utilized to constrain geometric properties and performance metrics, in order to avoid undesirable characteristics or infeasible configurations. Finally, a multi-objective aerostructural trim optimization is carried out, with comparison to a prior reusable launch vehicle concept.

I. Introduction

Fully reusable launch vehicles (RLV) have time and again proved to be a significant, and so far overwhelming technical challenge. Research and design of reusable two-stage-to-orbit (TSTO) vehicles has peaked and troughed since the 1930s, with its single-stage counterpart (SSTO) receiving more attention in the 1960s [1]. The step towards entirely reusable spacecraft provides an abundance of advantages, with the most notable being a drastic decrease in the cost of manufacturing and integration of partially reusable or single use components. Furthermore, a huge reduction in overall turnaround time between missions would vastly increase access to space for not only commercial purposes, but potentially transport and tourism markets also. With improved access being a constant high-priority topic at the time, NASA produced a report in 1994 [2], anticipating that full RLVs would replace the space shuttle by the late 2000s. Despite their early conception and promise to revolutionize the space market as a whole, a fully reusable orbital system has not yet been successfully deployed, with only sub-orbital or partially reusable systems currently in place. Many factors have contributed to this slower than anticipated progress, such as drastically reduced funding and general public interest around the turn of the century. Nevertheless, the various aerothermodynamic, propulsive, structural and mission specific challenges associated with the development of fully reusable launch vehicles cannot be understated.

Throughout research and conceptualization of SSTO or TSTO RLVs, the over-arching problem has been their inability to deliver a reasonable payload fraction to at least low Earth orbit [1, 3]; making costly development programs unattractive considering the small initial benefits in the best case, and risk of an infeasible design in the worst. With continued advancements in propulsion and materials however, commercially viable fully reusable launch vehicles with increasing payload fractions appear more feasible and realistic. Considering that no successful configuration exists yet, it is not surprising that organizations who have undertaken the challenge produce radically different designs; varying not only in size and shape, but in propulsive methods, take-off/landing approaches, and mission specifications, to name a few.

Many failed attempts exist in the pursuit of a fully reusable launch system, with a need for maturation of various technologies being a common theme amongst the dissolved projects. In 2003, Bayer [4] compared various rocket propelled vertical takeoff/vertical landing (VTVL), vertical takeoff/horizontal landing (VTHL), and horizontal takeoff/horizontal

---

*PhD Student, School of Engineering, University of Glasgow.

[†]Professor, School of Engineering, University of Glasgow.

[‡]Professor, Faculty of Aeronautics and Astronautics, Istanbul Technical University.

landing (HTHL) SSTO concepts that existed at the time; encompassing ballistic, wing-body and lifting body designs. Bayer pointed out the strong design sensitivities and risks that are present in the initial concept selection, emphasizing that often performance degradation throughout design iterations and increased fidelity of analysis can severely damage or completely negate their practical feasibility. The X-33/Venturestar (VTHL) RLV program [5] proved to be an excellent example of both the aforementioned themes. During a ground test of the system, a highly complex hydrogen tank design failed, affirming the need for technology maturation. As the X-33 design process matured itself, various alterations were deemed necessary, resulting in a drastically increased takeoff weight. A combination of these factors, among others, resulted in the termination of the X-33/Venturestar program, and provided a harsh warning to future SSTO/TSTO concepts.

A second but radically different design involved in the X-33 project was the VTVL Delta Clipper Experimental (DC-X) [6]. While not selected as the final design, multiple successful test flights were conducted as part of a separate project, demonstrating the capability of vertical landings and rapid turnaround time. While the DC-X program was also prematurely discontinued, in this instance following a catastrophic failure on landing during a test flight, its legacy is clear to see today, with various organizations employing the vertical landing approach for their RLV programs.

Completing the wide spectrum of concepts during this period of interest in space accessibility, the wing-body X-34 configuration [7] was developed as a low Earth orbit small payload launcher. It would be deployed from a carrier aircraft, reaching altitudes over 75000m, before returning to Earth via an unpowered re-entry/descent, and landing on a conventional runway. Much like the X-33/Venturestar project, the X-34 was cancelled prior to flight, but once again its legacy has provided a benchmark for future designs of carrier aircraft launched or HTHL small payload launchers and beyond.

Following these ambitious SSTO projects, organizations have tended towards more conservative TSTO developments, with a recent space boom being attributed to the successful reusable rocket capabilities demonstrated by SpaceX [8]. The recent report by Niederstrasser [9] detailed this further, with various organizations deciding to take on the final frontier as of late. While not all of these concepts are fully reusable ones, it is apparent in the current climate that reusability is the long term goal for the industry to move forward as a whole.

Advancements in high-speed propulsion systems promise to reduce the reliance on purely rocket based methods, which are highly inefficient at low altitudes. While utilization of air-breathing engines for use at low altitudes en route to space is not a new concept in itself [10], it was often shown to provide only marginal performance gains, if any, due to the increased structural requirements of the air-breathing system [1]. With the projected increase in efficiency of varying rocket/air-breathing propulsion configurations [11], an even more diversified set of RLV concepts have emerged. Regardless of the chosen engine architecture, structural weight and propellent storage remain key concerns, and the selection of propulsive method will inevitably have a large impact on the overall shape of the vehicle as a whole.

With uncertainty surrounding the optimal propulsion system configuration for future RLVs, this research aims to produce novel vehicle geometries through multidisciplinary analysis, from an arbitrary design space. The bounds of these variables may be influenced by the pre-determined system design details; such as propulsion methods, structural integrity, or payload requirements. These may enforce restrictions on geometric properties such as wingspan or internal volume, but as can be seen from the wide variety of prior and existing concepts, leave a range of properties still to be determined. Coupling this with the limited experience of successful high-speed applications, it is clear that much work is required in all aspects of the design and testing phases. Here, low-fidelity analysis methods are coupled with gradient-free optimization techniques, allowing thousands of configurations to be analyzed at relatively low computational cost. This allows multiple flight states to be considered, along with regions of the search space that may result in infeasible designs or those that contain undesirable characteristics, but that cannot be quantified a priori. Results from such optimizations should allow a wide variety of potential configurations to be analyzed based on the trade-off in their objective functions, before choosing a suitable candidate or candidates to continue the design process with.

In particular, this paper seeks to design a RLV wing configuration from a large search space, based on aerostructural and trim performance. Firstly, the aerodynamic and structural modelling methods employed are briefly outlined, followed by a discussion of the interface between the two disciplines, including the interpolation methods required in order to transfer data between them. The optimization method utilized is introduced, and its suitability to the problem summarized. Next, the overall architecture of the framework is described, followed by a discussion of the implemented design variables, as well as undesirable traits that may arise for a given set of variables, and how these are managed. Finally, results are shown for an aerostructural trim design optimization, in which the Orbital Sciences X-34 [12] RLV concept has been chosen as a benchmark. It is important to note that this configuration is not used as a starting point; it does however place reasonable limits on the design parameters and performance characteristics.

Key outcomes from this are the demonstration of the optimization framework as a whole, to produce realistic designs

in highly constrained, multi-disciplinary optimization, that requires convergence from a large number of aerostructural loops. Moreover, it is hoped that the quantification of undesirable and infeasible design characteristics will demonstrate the frameworks ability to handle a large search space, and produce novel, diverse results.

II. Methodology

A. Aerodynamic Modelling

Surface inclination methods such as modified-Newtonian[13], oblique shock-expansion[14], and tangent wedge/cone[15] have been chosen for this research, due to their ability to rapidly compute aerodynamic properties of arbitrary shapes. The latter two techniques assume an attached shock, which of course is not possible for certain Mach number and inclination angle combinations. All attached shock techniques therefore complete a check to ensure that they can be utilized in a given circumstance, with the use of a pre-loaded maximum θ-β-M database. In such cases where an attached shock is not possible, properties are calculated by the Modified-Newtonian method. This is due to Newtonian flow assuming a detached shock, and thus no inclination limits apply. In shadow regions, Prandtl-Meyer theory is utilized in a majority of cases, as it consistently provides increased accuracy over other methods. In special cases however, such as surfaces whose normals point in a similar direction to the freestream velocity vector, known as base regions; surfaces with a large expansion angle with respect to their previous panels; or in very high Mach number cases, different techniques must be applied. Here either Gaubeaud's base pressure formula[16], which is constant for a given flight state, or the Newtonian assumption of freestream conditions on shadow regions is used. Once again checks are put in place to ensure these special cases are treated appropriately, for example setting all panels with an inclination $\theta < -45°$ to base pressure. Viscous effects are estimated using Eckert's reference temperature method [17], with options of strip theory or streamline tracing for particle tracking. Further detail on the implemented methods, along with validation data can be found in [18].

B. Structural Modelling

As an initial estimation of static wing elasticity, a simple wing-box definition is reduced to a beam model. In such structures, the upper and lower skins primarily carry the bending loads on the wing, with span-wise spars supporting shear loads. Defining the wing structure in this manner allows a straightforward box model to be created, in which cross sectional properties can be determined easily. Additional stiffness is provided through stringers, distributed evenly over both upper and lower skins. As in [19], stringers at the front and rear spars are cross coupled in terms of area, while inner stringer areas are defined by a single variable. Wing-box segments are separated by beam nodes, as shown in fig. 1. The average chord of each segment is thus used in the cross-section property computation, resulting in a beam model that is representative of a series of cuboid shaped wing-box segments. A portion of the structure is also assumed to lie inboard of the wing aerodynamic mesh, representing the fuselage joint. Therefore, the innermost node is clamped, while the second is semi-flexible [20]. Since the physical attributes of the wing-box are computed prior to simplification, the volume of each component and thus overall weight of the wing-box can also be determined. From here, the total wing weight is estimated using an empirical method [21]. The loads produced by the wing structure are distributed uniformly along the elastic axis and applied to the element nodes by computing the work-equivalent nodal forces and moments [22].

Once the cross-section properties and weight estimations have been computed, the wing-box segments are reduced to a single span-wise beam, connected end-to-end, allowing beam element stiffness matrices to be collated globally on block diagonals. The linear system $\mathbf{Ku} = \mathbf{f}$ is then solved using Gaussian elimination, where $\mathbf{K}$ is the global stiffness matrix, $\mathbf{f}$ is the vector of forces and moments provided from the aerodynamic solver, along with weight estimations, and $\mathbf{u}$ is the resulting vector of structural displacements and rotations.

To ensure that the structure has not failed under the aerodynamic loads produced in a given flight state, stress distribution and failure criteria are calculated for each beam element using the equations provided in [21]. Here, both failure due to material yield and failure due to buckling are considered. To determine the maximum allowable stress that a given structure can undergo before it fails, the equations from [23] are utilized. Assuming the entire structure is made of a single metal alloy, its mechanical properties can be used in determining these allowables [24]. Upper and lower panel buckling is calculated through the stiffened panel efficiency method, presented in [25], in which an efficiency factor of 0.8 is adopted, assuming a realistic z-stringer joint is present in both panels. Shear buckling is also considered for the spar webs, again discussed by Niu [25]. A constant safety factor of 1.5 is applied to the maximum stresses, and

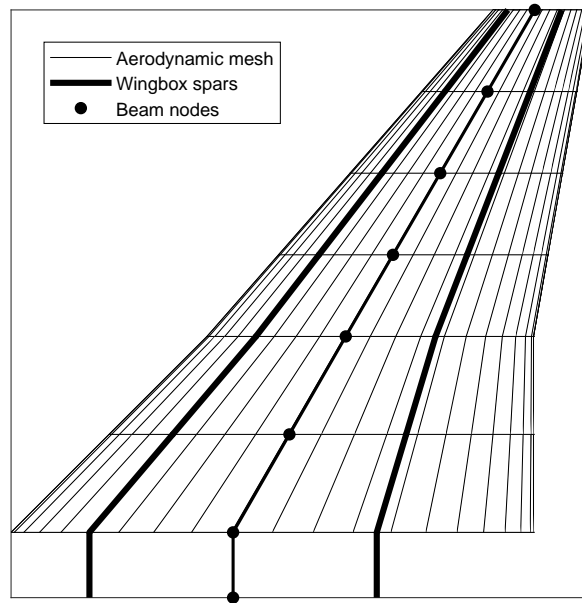flight state analysis terminated if any wing-box element is deemed to have failed.

Fig. 1   Aerodynamic and structural definitions

C. Aerostructural Interface

Coupling the aerodynamic and structural solvers is achieved through the use of Gauss-Seidel fixed-point iterations. This method allows each solver to run in sequence, using the data gathered from the previous output of the other, until there are no further changes in their respective outputs. This process is completed as follows: The aerodynamic module is run initially, and once forces on individual panels of the undeformed mesh have been computed, they will be transferred to the structural solver, where equivalent loads on the beam nodes are calculated. Combining these forces and moments with those derived from the estimated wing weight then allows the resulting beam displacements and rotations to be found. The structural mesh motion is translated to the aerodynamic mesh, where the process repeats until convergence. With low-fidelity aerodynamic methods being employed, the aerostructural solution can be considered to have converged once the aerodynamic mesh motion Δw, that is the change in mesh from the previous iteration, becomes negligible. In this work, we assume convergence when $||\Delta w|| < 10^{-6}$.

The rigid link method [26] has been employed for use in both virtual work transfer of forces and moments, along with mesh motion. Here, coupling the two domains is achieved by finding the nearest structural node to a given node on the fluid surface, and using the vector connecting these two points to transfer information. The overriding reason for this is the choice of structural model, in this case a single discretized beam. In terms of structural displacements and rotations, this is completed as follows:

$$\mathbf{u}_A = \mathbf{u}_S + \theta_S \times \mathbf{r} \tag{1}$$

Where $\mathbf{u}_S$ and θ_S are the displacements and rotations of the donating structural node, $\mathbf{r}$ is the vector defined from the structural node to the fluid node, and $\mathbf{u}_A$ is the resulting displacement of the aerodynamic node. Similarly, the rigid link vector is used in the translation of forces and moments from the fluid grid to the structural load vector through virtual work. It is important that the rigidity of this vector is emphasized, meaning that when an iterative scheme is applied, $\mathbf{r}$ should only be calculated in the pre-processing phase with the undeformed meshes. This method is commonly used in high-fidelity analyses [20, 27]. However recently, it has also been used for low-fidelity coupling [21, 28]. Both of the referenced works use a simple idealized beam model for the wing structure, and exploit the rigid link method by aligning the beam nodes with the fluid mesh in the span-wise direction. This means that finding the closest structural

4

node to a given fluid point can be bypassed, and allows node specific expressions to be derived for loading and mesh motion transfer [28].

As arbitrary wing shapes and structures will be created and analyzed in a large design space, population based optimization, with many infeasible designs expected in the early stages, an efficient interface is required between the two disciplines. Therefore, the process is accelerated with a version of Aitken's [29] relaxation parameter, ω, which is applied to the structural displacements and rotations. This method has been used extensively in fluid-structure interaction applications [28, 30, 31]. Calculation of the parameter is carried out through the use of structural displacements from previous and current iterations to accelerate the systems convergence. Once found, it relaxes the structural displacements of the current iteration, and thus the motion of the aerodynamic mesh. Since a previous cycle is required in order to calculated the parameter, a value of $\omega = 0.5$ is used for the initial cycle.

D. Optimization Method

With a large design space desired, along with low-fidelity analysis techniques employed, a population based, heuristic optimization algorithm allows efficient exploration of the search space. Particle swarm optimization (PSO) has been chosen for this work, due to the design space being almost entirely continuous. The specific version of the PSO algorithm used is similar to that of OMOPSO [32], which includes various methods of particle mutation, selection of the global best based on the dominating characteristics of Pareto front particles, and various other methods that focus on creating a diverse set of results [18].

While the design space in this work is mostly continuous, the output cost functions for a given set of designs are not. This is due to the fact that analyzed configurations may have attributes that are physically undesirable, but that may be seen as desirable to the optimizer, and cannot be constrained or calculated prior to analysis. In such cases, an exponential based penalty function is used, which compares vehicle characteristics to predefined minimum and/or maximum values, and applies a penalty to the cost function values depending on how far out with the boundaries a violating attribute lies. This method allows the optimizer to analyze infringing configurations without seeing them as optimal, while also not disregarding them entirely. Furthermore, smoothing the cost functions in this manner allows the optimizer to tend towards non-violating values, improving overall convergence.

III. Computational Framework

A. Overall Architecture

The overall architecture of the described framework is shown in fig. 2. Particle initialization can be performed randomly between variable boundaries or through the use of Latin hypercube sampling. Any user-defined constraints on the design variables are then applied, while also ensuring particle positions remain within the set boundaries throughout the optimization. Once constrained, the particles are passed to the objective functions, where their design variables are used to create physical configurations.

Two loops are performed within the cost function; the outer attempting to find the trim angle of attack, and the inner solving the aerostructural system for the current angle. In terms of trim analysis, the lift force for a given flight state is compared to the total configuration weight, and the angle of attack updated accordingly. At a given inclination angle, aerodynamic forces acting on the undeformed mesh are computed, which are transferred to the structural solver to calculate displacements and rotations. These deformations are used to displace the aerodynamic mesh, and this process is repeated until either convergence or failure criteria is met. If converged, overall aerodynamic and structural properties are gathered, and a check is performed to determine if the aircraft is at trim conditions. Until this stability criteria has been met, the angle of attack is updated; the aerodynamic and structural meshes are initialized to their undeformed state; and the aerostructural loop is repeated. Upon convergence of the entire aerostructural trim system, violation characteristics are computed, and any penalties added to the final cost function values.

To reduce the number of outer loop iterations, boundaries are set on the allowable trim angle of attack range, and the final α_{trim} value is only computed to three decimal places. Furthermore, if the wing structure is deemed to have failed at any point within this process, the cost function is continued with a rigid airframe. Previously, the cost function would have been terminated entirely, and the configuration marked as infeasible. However, this caused a large amount of noise in the cost function, with relatively similar designs having potentially optimal and infeasible designations. By allowing analysis to continue with a structurally incapable design, comparisons can be drawn amongst the remaining performance metrics, and penalties applied purely based on the structural infeasibility.
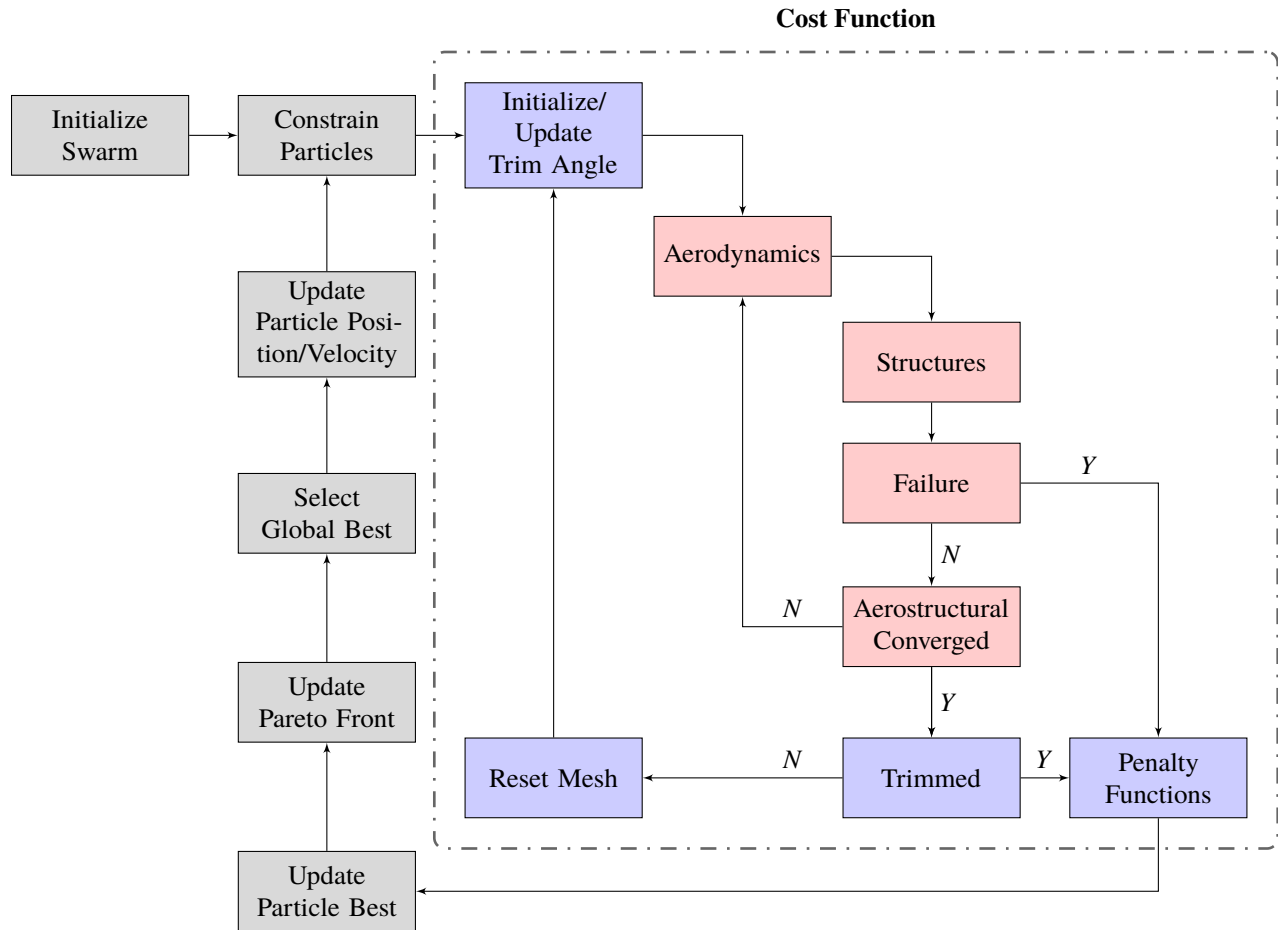
Cost Function

Fig. 2   **Multi-objective aerostructural trim particle swarm optimization**

After all particle cost function values have been calculated in a given iteration, they are compared to that of the previous best cost function found by that particle, and updated accordingly. Similarly, these particle best values are compared to those of the Pareto front, with particle positions added or removed as appropriate. Global best particles are selected based their dominance of the population during the current iteration, which are used to amend particle positions and velocities for the next iteration. Finally, mutation functions are applied before particle variables are passed to the constraint manager, where the optimization loop begins again. At present, there are no widely accepted methods that define convergence of a multi-objective population based optimizer. Therefore, the PSO algorithm is run for a set number of iterations, defined by the user.

B. Description of Design Variables

Before configurations in a given design space can be analyzed and optimized, a vehicle generator is required. Such a program must be able convert parametrically defined variables into full wing-body vehicles. Furthermore, it must not only be capable of reliably producing such configurations given any set of design variables within their respective boundaries, but consistently discretize the various components to a high enough degree that multi-disciplinary analysis can be considered accurate. This process requires combination of the components into a single non-intersecting, air tight surface, in which any inner surfaces are discarded, and a consistent discretization is enforced at the boundaries of merging parts.

On the other hand, it is important that the variables required for creation are chosen carefully based on the overall research scope, and therefore the desired optimization criteria. Considering the exploratory nature of this work, the majority of cases allow a high level of flexibility in the choice of optimization variables, and their respective boundaries.
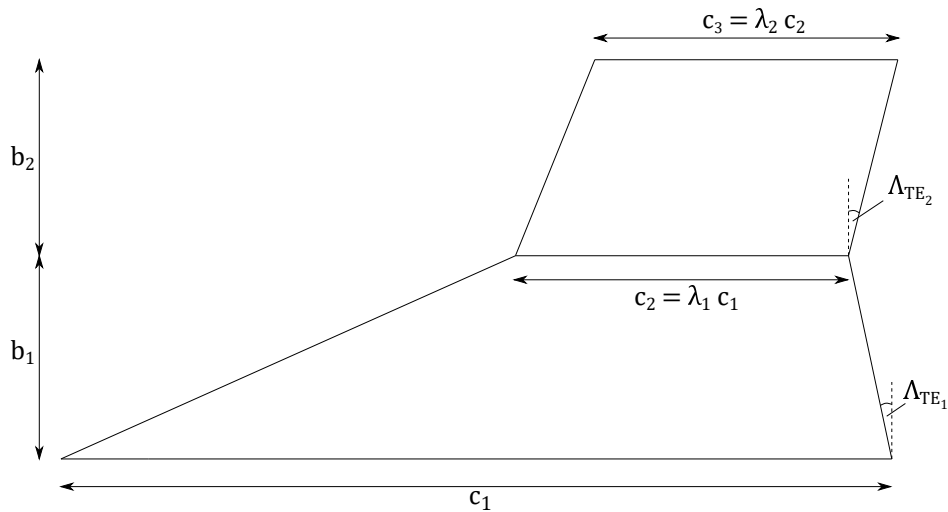
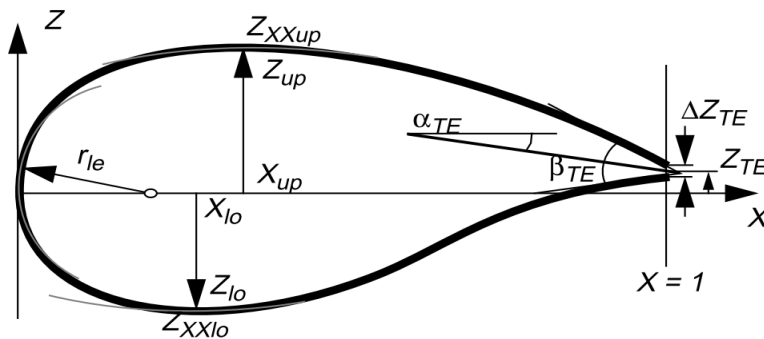**Fig. 3   Planform wing design variables**

Fig. 4   PARSEC geometry definition [33]

This is desirable in conceptual design, and realized by the utilization of low-fidelity cost function analysis, providing a relatively small computational cost for a given design. Nevertheless, if optimization variables do not have a clear and consistent definition, or introduce large non-linearities to the resulting objective functions, the algorithm may fail to consistently converge on globally optimal solutions.

1. Wing Planform

An arbitrary number of separate wing partitions can be used to create a single wing. Each partition is defined by five parameters: dihedral, taper ratio, trailing edge sweep, span, and two-dimensional aerofoil section. Of course an initial root chord is required, which can be an optimization variable directly, or a ratio of fuselage length. The decision to use trailing edge sweep as a design parameter instead of defining it at the quarter chord or leading edge was to ensure that control surfaces were not made ineffective by high rearward sweep or large sweep discrepancies between partitions. Such a definition may result in undesirable sweep elsewhere on the wing chord, which can be easily calculated and constrained in the analysis phase. An example of the design variables used to define a two partition wing is shown in fig. 3.

2. Aerofoil

Initially, Bézier curves were selected for the task of aerofoil generation alone. However, while being a robust and versatile approach, there was something left to be desired in terms of their design variables. Since no direct control can be had over the aerofoils physical properties, the aerofoil specific method PARSEC[33], was implemented in this work, with a comparison of these approaches for global aerofoil design optimization to be the subject of future work. This

7

approach creates 6th order upper and lower polynomials based on geometric characteristics such as maximum thickness, leading edge radius and trailing wedge angle. These polynomials are calculated as follows:

$$z = \sum_{i=1}^{6} a_i x^{\left(i-\frac{1}{2}\right)} \tag{2}$$

Where z is given vertical location of the curve at prescribed x coordinates, which are cosine spaced in order to properly capture the aerofoil geometry at the extremities. The coefficients a_i, and therefore eq. (2), are computed for both upper and lower surfaces as a result of solving the linear system of equations below, which contain the various geometric parameters:

$$\begin{bmatrix} 1 & 1 & 1 & 1 & 1 & 1 \\ X_u^{\frac{1}{2}} & X_u^{\frac{3}{2}} & X_u^{\frac{5}{2}} & X_u^{\frac{7}{2}} & X_u^{\frac{9}{2}} & X_u^{\frac{11}{2}} \\ \frac{1}{2} & \frac{3}{2} & \frac{5}{2} & \frac{7}{2} & \frac{9}{2} & \frac{11}{2} \\ \frac{1}{2}X_u^{-\frac{1}{2}} & \frac{3}{2}X_u^{\frac{1}{2}} & \frac{5}{2}X_u^{\frac{3}{2}} & \frac{7}{2}X_u^{\frac{5}{2}} & \frac{9}{2}X_u^{\frac{7}{2}} & \frac{11}{2}X_u^{\frac{9}{2}} \\ -\frac{1}{4}X_u^{-\frac{3}{2}} & \frac{3}{4}X_u^{-\frac{1}{2}} & \frac{15}{4}X_u^{\frac{1}{2}} & \frac{35}{4}X_u^{\frac{3}{2}} & \frac{63}{4}X_u^{\frac{5}{2}} & \frac{99}{4}X_u^{\frac{7}{2}} \\ 1 & 0 & 0 & 0 & 0 & 0 \end{bmatrix} \begin{bmatrix} a_{u_1} \\ a_{u_2} \\ a_{u_3} \\ a_{u_4} \\ a_{u_5} \\ a_{u_6} \end{bmatrix} = \begin{bmatrix} Z_{te} + \frac{1}{2}\Delta Z_{te} \\ Z_u \\ tan\left(\alpha_{te} - \frac{1}{2}\beta_{te}\right) \\ 0 \\ Z_{xx_u} \\ \sqrt{2r_{le_u}} \end{bmatrix} \tag{3}$$

$$\begin{bmatrix} 1 & 1 & 1 & 1 & 1 & 1 \\ X_l^{\frac{1}{2}} & X_l^{\frac{3}{2}} & X_l^{\frac{5}{2}} & X_l^{\frac{7}{2}} & X_l^{\frac{9}{2}} & X_l^{\frac{11}{2}} \\ \frac{1}{2} & \frac{3}{2} & \frac{5}{2} & \frac{7}{2} & \frac{9}{2} & \frac{11}{2} \\ \frac{1}{2}X_l^{-\frac{1}{2}} & \frac{3}{2}X_l^{\frac{1}{2}} & \frac{5}{2}X_l^{\frac{3}{2}} & \frac{7}{2}X_l^{\frac{5}{2}} & \frac{9}{2}X_l^{\frac{7}{2}} & \frac{11}{2}X_l^{\frac{9}{2}} \\ -\frac{1}{4}X_l^{-\frac{3}{2}} & \frac{3}{4}X_l^{-\frac{1}{2}} & \frac{15}{4}X_l^{\frac{1}{2}} & \frac{35}{4}X_l^{\frac{3}{2}} & \frac{63}{4}X_l^{\frac{5}{2}} & \frac{99}{4}X_l^{\frac{7}{2}} \\ 1 & 0 & 0 & 0 & 0 & 0 \end{bmatrix} \begin{bmatrix} a_{l_1} \\ a_{l_2} \\ a_{l_3} \\ a_{l_4} \\ a_{l_5} \\ a_{l_6} \end{bmatrix} = \begin{bmatrix} Z_{te} - \frac{1}{2}\Delta Z_{te} \\ Z_l \\ tan\left(\alpha_{te} + \frac{1}{2}\beta_{te}\right) \\ 0 \\ Z_{xx_l} \\ -\sqrt{2r_{le_l}} \end{bmatrix} \tag{4}$$

Table 1 shows the minimum and maximum boundaries of these geometric properties that were utilized for the given optimization. Note that aerofoil sections are generated non-dimensionally, before being dimensionalized by the chord at their location within the wing during the assembly phase.

Table 1   PARSEC variable boundary definitions

Property	Minimum	Maximum
r_{le}	0.005	0.1
X_u	0.2	0.7
Z_u	0.02	0.12
Z_{xx_u}	-1.2	0
X_l	0.2	0.7
Z_l	-0.08	-0.02
Z_{xx_l}	0	1.2
Z_{te}	-0.02	0.02
ΔZ_{te}	0	0.02
α_{te}	-25	2
β_{te}	3	40

3. Wing-box

Nine variables are required to create the rectangular wing-box structure as shown in fig. 5. The position of the front and rear spars are required, in terms of non-dimensional chord, as well as constant values for spar and web thickness, $t_{s,w}$. The number of inner stringers has been included as a variable, N, to allow for a more versatile design space, which
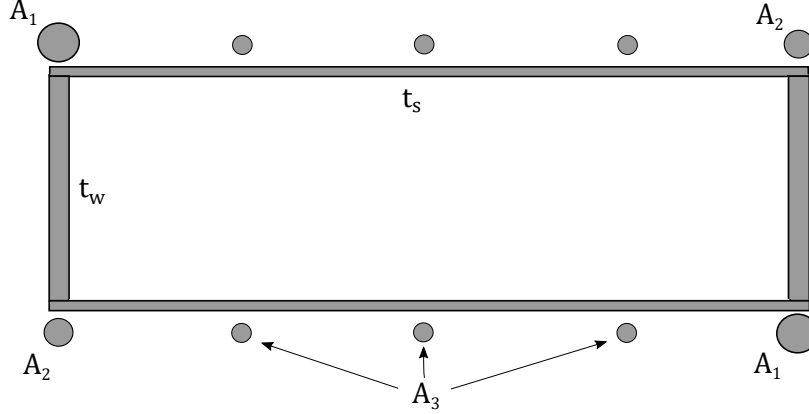
8

Fig. 5   Wing box thickness and stringer area variables

is the only discrete variable in the optimization. As the stringers will be idealized as booms, three areas are required for the two sets of cross-coupled stringers at the spars, $A_{1,2}$, along with one variable that defines the area of all those located within, A_3. Finally, the rib pitch is included as an optimization variable, as this is a necessary parameter in the stiffened panel efficiency method [25]. From these features, the wing-box cross-sectional properties can be calculated using the following equations [19]:

$$A = 2 \cdot (t_s \cdot c + t_w \cdot h + A_1 + A_2 + N \cdot A_3) \tag{5}$$

$$I_1 = 2 \cdot \left((t_w \cdot h + A_1 + A_2) \cdot \frac{c^2}{4} + \frac{c^3 \cdot t_s}{12} + A_3 \cdot c_3 \right) \tag{6}$$

$$I_2 = 2 \cdot \left(\frac{t_w \cdot h^3}{12} + (t_s \cdot c + A_1 + A_2 + N \cdot A_3) \cdot \frac{h^2}{4} \right) \tag{7}$$

$$J = 2 \cdot \left(\frac{c^2 \cdot h^2 \cdot t_w \cdot t_s}{c \cdot t_w + h \cdot t_s} \right) \tag{8}$$

Where c and h are the chord and height of the wing-box, and c_3 is the summed squared chord-wise distance of every inner stringer from the neutral axis. Note that since the box is rectangular, all stringers will be equidistant from the neutral axis in terms of height, hence why they have been grouped together in eq. (7). Furthermore, note that ribs are not included in the wing-box properties calculation, however their weight contribution is estimated empirically [23].

IV. Results & Discussion

To demonstrate the capability of the overall framework, a multi-objective, multi-flight state optimization was conducted, and compared to that of the X-34 configuration. Three objectives were sought to be minimized across Mach numbers of 3 and 6, with the remaining flow properties defined by that of experiments carried out in [34]. The overall optimization problem is defined in table 2, and results shown in the form of a Pareto front in fig. 6. Particles are coloured in order to demonstrate their relative objective function values versus the rest of the front. Here, red indicates a low drag coefficient, green tends towards minimal trim angle, and blue shows reduced wing mass. As mentioned previously, the X-34 configuration has been used a baseline to provide constraints on designs, and present a comparison for optimal results. In particular, since the X-34 was designed to be launched from a carrier aircraft, strict geometric requirements have been placed on candidate designs, along with those demanding a maintenance or improvement in terms of performance. The optimization was run for 600 iterations with 1200 particles across 8 cores, and completed in approximately 72 hours.

Note that no attempt has been made to model the X-34 structure, and thus its performance is based on a rigid airframe. Furthermore, only the wing and body sections have been modelled in this instance. The original wing mass is an estimation based on the overall structural weight of the vehicle, and the empty weight has been utilized in the trim computation, implying an unpowered descent phase.

Table 2   Tri-objective optimization problem definition

		Comments
Minimize	$C_{D_{trim}}$	Optimize trim angle and drag coefficient at trim
	α_{trim}	based on maximum respective values from both
	m_{wing}	flight states, and overall wing mass
Subject to	$L \approx W$	
	$C_m \approx 0$	Trim conditions
	$C_{m_\alpha} < 0$	
	$C_{L_{trim}} \geq C_{L_{base}}$	Improve or maintain baseline trim lift coefficient
	$0.5\, A_{base} \leq A_{wing} \leq 1.5\, A_{base}$	Constrain wing planform area and wing root, tip, and trailing
	$0.5\, t_{base} \leq t_{wing} \leq 1.5\, t_{base}$	edge thickness
	$\frac{dt}{db} \leq 0$	Wing thickness cannot increase outboard
	$b \approx b_{base}$	Wingspan within 2% of baseline
	$r_{le} \geq r_{base}$	Ensure minimum leading edge for heating requirements
	$30° \leq \Lambda_{le} \leq 80°$	
	$0.15 \leq c_{t_{max}} \leq 0.65$	Non-dimensional chord location of maximum aerofoil thickness
	$\left(\frac{dt}{dc}\right)_{t < t_{max}} \geq 0$	Aerofoil thickness cannot decrease up to maximum thickness
	$\left(\frac{dt}{dc}\right)_{t > t_{max}} \leq 0$	Aerofoil thickness cannot increase after maximum thickness
	Failure ≤ 0	Failure criteria for all skin panels & spar webs for every aerostructural loop

Three optimal configurations have been extracted from the 58 found on the Pareto front, and are shown in fig. 7 along with the baseline shape. Furthermore, performance characteristics are compared in table 3, again shown in terms of maximum values across the two flight states. Note that this generally corresponds to Mach 3 in terms of force and moment coefficients, and Mach 6 in terms of trim angle. Similarities can be drawn from the aerofoil shapes presented in all cases, particularly in configurations a) and b), along with similar planform shapes in a) and c). However, stark contrasts are observed from their objective functions. Unsurprisingly, configuration b) provides a minimal mass option, due to its reduced wing area. Furthermore, despite their geometric similarities, configuration a) demonstrates a low drag coefficient design, with c) performing best in terms of trim angle.

Much like the baseline shape, thinner aerofoils are generally present at the root of designs, due to their large inboard chord. A drastic increase in lift coefficient compared to the baseline can also be observed from the three designs, despite a reduction in trim angle. However, the large sweep of the X-34 strake, and thus reduction in drag that it provides, is not seen across the resulting configurations. Furthermore, in an attempt to maintain structural integrity at such high speeds, increased mass values are present across the Pareto front versus that of the X-34 estimation. A combination of these properties point to potential inaccuracies in weight prediction, since the X-34 has a considerably larger wing area than almost all of the resulting designs.

Various nuances are present in the remaining Pareto front designs, particularly in terms of structural definition and aerofoil shape. However, many of the geometric characteristics discussed can also be seen in multiple configurations, showing convergence tendencies for the given problem. Structurally, only a few configurations contain more than one inner stringer, demonstrating a preference for thicker spar panels and cross-coupled stringers, rather than additional stiffening inboard. Of course, the low-fidelity structural model may be a cause of this results, since structural failure plays a large role in the optimization process. Further flexibility is therefore desired in the wing-box design, to ensure fewer failing configurations, and a broader search space of feasible structures.

V. Conclusions

Presented is a low-fidelity, large search space global design optimization framework for super-hypersonic vehicles. Low-fidelity surface inclination methods have been employed for aerodynamic analysis, with a simple wing-box model being reduced to a single discretized beam to approximate structural elasticity. Gauss-Seidel fixed-point iterations have been utilized to couple the aerostructural system, with Aitken relaxation used to accelerate convergence. Particle swarm has been chosen as the optimization algorithm, due to its superior handling of continuous, large design space
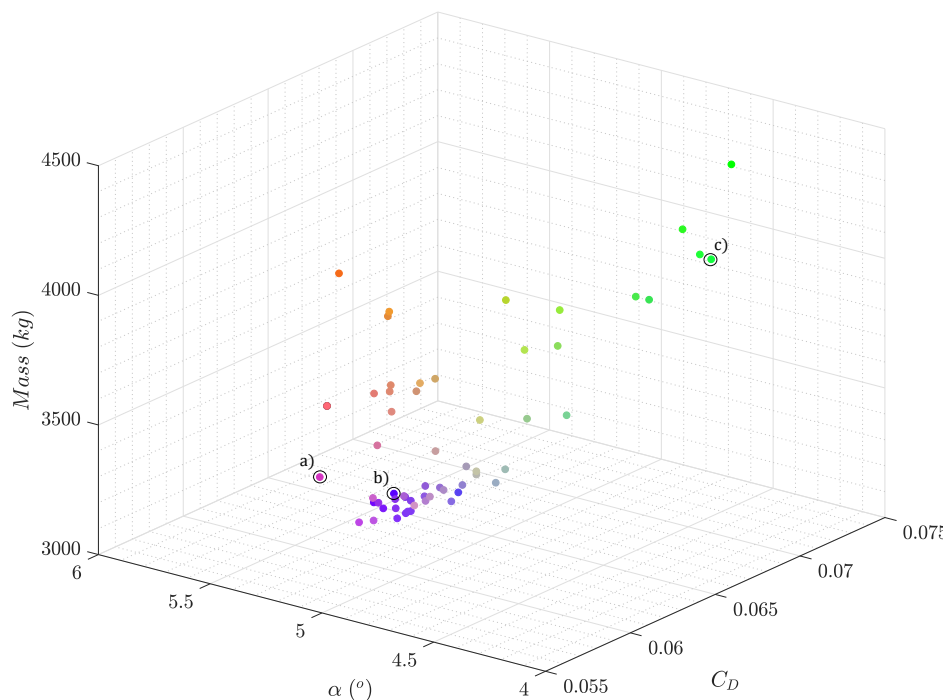
Fig. 6   Aerostructural trim optimization Pareto front with rigid baseline comparison

Table 3   Optimal design performance characteristics

	Baseline	Configuration a)	Configuration b)	Configuration c)
$C_{D_{trim}}$	0.0402	0.0551	0.0625	0.0702
$\alpha_{trim}(°)$	5.244	4.983	5.231	4.326
$m_{wing}(kg)$	3000	3800	3091	4430
$C_{L_{trim}}$	0.0565	0.069	0.0779	0.0724
$C_{m_{trim}}$	-0.0173	-0.0114	-0.0164	-0.0007

problems over gradient-based or other gradient-free methods. The combination of these tools has produced a versatile design optimization system capable of handling a broad design space, and large number of function evaluations, without significant computational cost.

A detailed description of the design variables has been provided, with explanation of a penalty approach for constraint management and undesirable characteristics or infeasible designs. A multi-objective, multi-flight state aerostructural trim optimization has been performed, with comparison to the wing-body X-34 RLV configuration, and select Pareto front designs shown. A diverse set of configurations have been produced, proving the optimizers capability in handling large design spaces and highly non-linear objective functions. This is due to its flexibility in allowing undesirable or infeasible characteristics to be analyzed and appropriately quantified. Baseline improvements can generally be found in terms of trim angle and lift coefficient; however mass estimation has been highlighted as a crucial limiting factor in producing lower drag and overall wing weight. Future work will seek to improve upon this, and provide higher fidelity structural definitions, to allow an increased level of control. Furthermore, studies will seek to optimize full wing-body RLV designs, with and without constraints introduced by a baseline configuration, along with the implementation of lifting body and capsule design spaces.
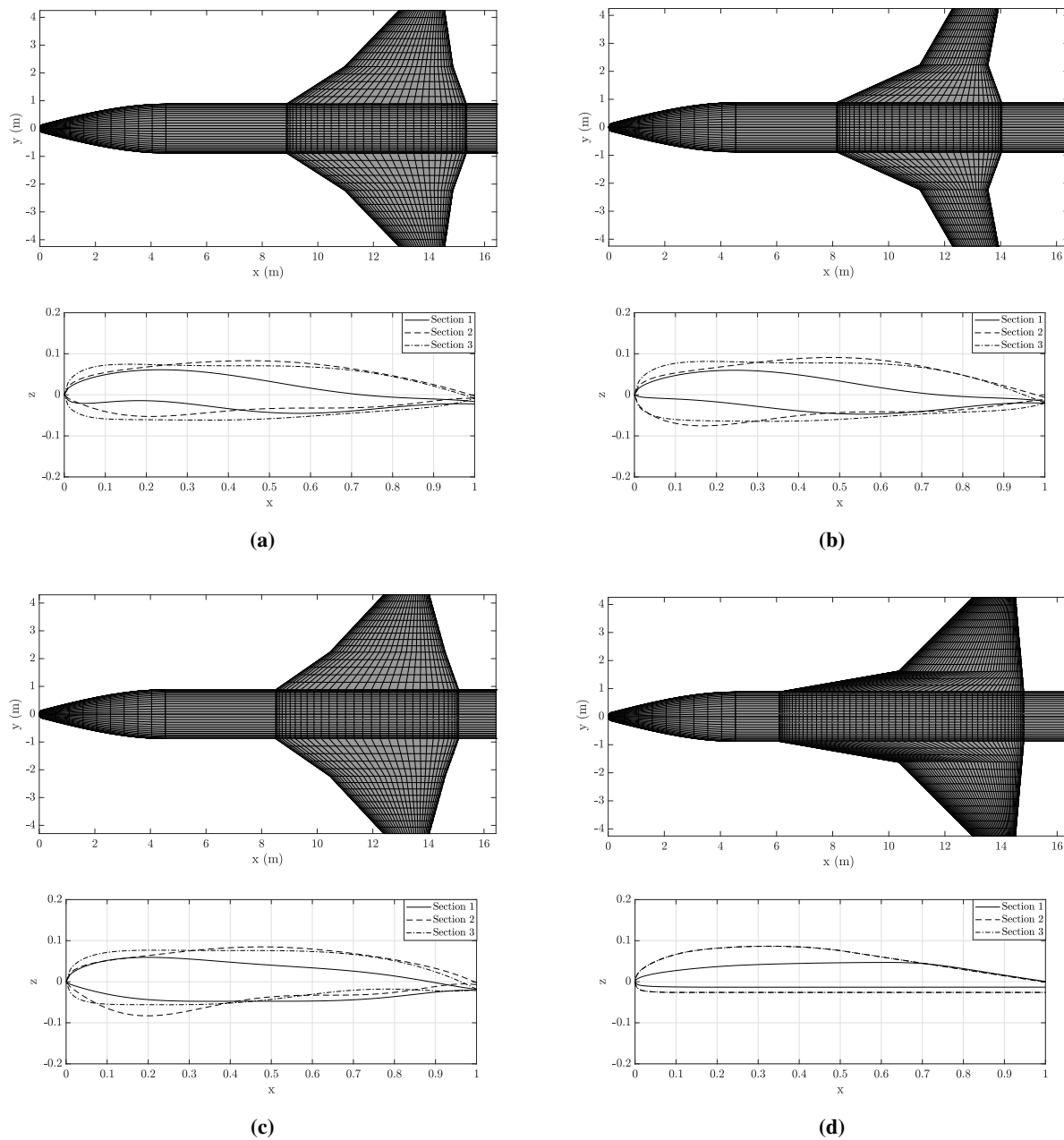
Fig. 7   Selected Pareto front configurations (a - c), and baseline (d), with non-dimensional aerofoil sections shown from root (1), to partition joint (2) and tip (3)

References

[1] Dorrington, G. E., "Performance of air-breathing single-stage-to-orbit vehicles," *Acta Astronautica*, Vol. 22, 1990, pp. 17–41.

[2] "Access to Space Study," Tech. rep., Office of Space Systems Development, NASA Headquarters, Washington, 1994.

[3] Bentley, M., *Spaceplanes*, Springer, 2009.

[4] Bayer, M. J., "Comparative Assessment of Rocket-Propelled Single-Stage-to-Orbit Concepts," *Journal of Spacecraft and Rockets*, Vol. 40, No. 2, 2003, pp. 273–278.

[5] Baumgartner, R. I., "Venturestar™ single stage to orbit reusable launch vehicle program overview," *Space technology and applications international forum (STAIF - 97)*, Vol. 1033, 1997, pp. 1033–1040.

[6] Freeman, D. C., Talay, T. A., and Austin, R. E., "Reusable launch vehicle technology program," *Acta Astronautica*, Vol. 41, No. 11, 1997, pp. 777–790.

[7] Miller, C. G., "Development of X-33/X-34 Aerothermodynamic Data Bases: Lessons Learned and Future Enhancements," Tech. rep., 1999.

[8] Reddy, V. S., "The SpaceX Effect," *New Space*, Vol. 6, No. 2, 2018, pp. 125–134.

[9] Niederstrasser, C., "Small Launch Vehicles A 2018 State of the Industry Survey," Tech. rep., Northrop Grumman Corporation, 2018.

[10] Huber, W. G., "Post-Saturn Launch Vehicle Study (Part II) Condensed Summary Report," Tech. rep., 1964.

[11] Preller, D., and Smart, M. K., "Reusable Launch of Small Satellites Using Scramjets," *Journal of Spacecraft and Rockets*, Vol. 54, No. 6, 2017, pp. 1317–1329.

[12] Fuhrmann, H. D., Hildebrand, J., Lalicata, T., and Corporation, O. S., "Aerothermodynamic Overview , X-34," *Journal of Spacecraft and Rockets*, Vol. 36, No. 2, 1999, pp. 153–159.

[13] Lees, L., "Hypersonic Aerodynamics," *Fifth Internation Aeronautical Conference*, Inst. of Aeronautical Sciences, New York, Los Angeles, 1955, pp. 241–276.

[14] Eggers, A. J., "The Generalized Shock-Expansion Method and Its Application to Bodies Traveling at High Supersonic Air Speeds," *Journal of the Aeronautical Sciences*, Vol. 22, No. 4, 1955, pp. 231–238.

[15] Dejarnette, F. R., Cheatwood, F. M., Hamilton, H. H., and Weilmuenster, K. J., "A review of some approximate methods used in aerodynamic heating analyses," *Journal of Thermophysics and Heat Transfer*, Vol. 1, No. 1, 1987, pp. 5–12.

[16] Guidi, A., Chu, Q. P., Mulder, J. A., and Buursink, J., "Implementation of an Aerodynamic Toolbox in a Reentry Flight Simulator," *Journal of Spacecraft and Rockets*, Vol. 40, No. 1, 2003, pp. 138–141.

[17] Eckert, E., "Engineering relations for heat transfer and friction in high-velocity laminar and turbulent boundary-layer flow over surfaces with constant pressure and temperature," *Transactions of the ASME*, Vol. 78, No. 6, 1956, pp. 1273–1283.

[18] Cusick, A., and Kontis, K., "Creation of Design and Analysis Tools for Large Design Space Reusable Launch Vehicle Shape Optimization," *AIAA AVIATION Forum*, Dallas, Texas, 2019.

[19] Bindolino, G., Ghiringhelli, G., Ricci, S., and Terraneo, M., "Multilevel Structural Optimization for Preliminary Wing-Box Weight Estimation," *Journal of Aircraft*, Vol. 47, No. 2, 2010, pp. 475–489.

[20] Brooks, T. R., Kenway, G. K. W., and Martins, J. R. R. A., "Benchmark Aerostructural Models for the Study of Transonic Aircraft Wings," *AIAA Journal*, Vol. 56, No. 7, 2018, pp. 2840–2855.

[21] Elham, A., and van Tooren, M. J. L., "Tool for preliminary structural sizing, weight estimation, and aeroelastic optimization of lifting surfaces," *Journal of Aerospace Engineering*, Vol. 230, No. 2, 2016, pp. 280–295.

[22] Chauhan, S., and Martins, J. R. R. A., "Low-fidelity aerostructural optimization of aircraft wings with a simplified wingbox model using OpenAeroStruct," *EngOpt 2018 Proceedings of the 6th International Conference on Engineering Optimization*, Springer, Lisboa, 2018, pp. 418–431.

[23] Elham, A., La Rocca, G., and van Tooren, M. J. L., "Development and implementation of an advanced, design-sensitive method for wing weight estimation," *Aerospace Science and Technology*, Vol. 29, 2013, pp. 100 – 113.

[24] MIL-HDBK-5G, "Military Handbook, Metallic Materials and Elements for Aerospace Vehicle Structures," , 1994.

[25] Niu, M. C. Y., *Airframe Stress Analysis and Sizing*, 2nd ed., Commit Press Ltd, Hong Kong, 1999.

[26] Brown, S., "Displacement extrapolations for CFD+CSM aeroelastic analysis," *38th Structures, Structural Dynamics, and Materials Conference*, AIAA, Reno, Nevada, 1997.

[27] Martins, J. R. R. A., Alonso, J. J., and Reuther, J. J., "A Coupled-Adjoint Sensitivity Analysis Method for High-Fidelity Aero-Structural Design," *Optimization and Engineering*, Vol. 6, 2005, pp. 33–62.

[28] Jasa, J. P., Hwang, J. T., and Martins, J. R. R. A., "Open-source coupled aerostructural optimization using Python," *Structural and Multidisciplinary Optimization*, Vol. 57, 2018, pp. 1815–1827.

[29] Irons, B. M., and Tuck, R. C., "A VERSION OF THE AITKEN ACCELERATOR FOR COMPUTER ITERATION," *INTERNATIONAL JOURNAL OF NUMERICAL METHODS IN ENGINEERING*, Vol. I, 1969, pp. 275–277.

[30] Küttler, U., and Wall, W. A., "Fixed-point fluid-structure interaction solvers with dynamic relaxation," *Computational Mechanics*, Vol. 43, 2008, pp. 61–72.

[31] Kennedy, G. J., and Martins, J. R. R. A., "Parallel Solution Methods for Aerostructural Analysis and Design Optimization," *13th AIAA/ISSMO Multidisciplinary Analysis Optimization Conference*, Fort Worth, 2010.

[32] Sierra, M. R., and Coello Coello, C. A., "Improving PSO-based Multi-Objective Optimization using Crowding, Mutation and e-Dominance," *International Conference on Evolutionary Multi-Criterion Optimization*, 2005, pp. 505–519.

[33] Sobieczky, H., "Parametric Airfoils and Wings," *Notes on Numerical Fluid Mechanics*, Vol. 68, 1998, pp. 71 – 88.

[34] Brauckmann, G. J., "X-34 Vehicle Aerodynamic Characteristics," *Journal of Spacecraft and Rockets*, Vol. 36, No. 2, 1999, pp. 229–239.